# Low Driving Voltage Lithium Niobate Metasurface Electro-Optical Modulator Operating in Free Space

AYMAN HOBLOS,[1,*] NADÉGE COURJAL,[1] MARIA P. BERNAL,[1] AND FADI I. BAIDA[1]

[1] Institut FEMTO-ST, UMR CNRS 6174, Université Bourgogne Franche-Comté, 25030 Besançon, France
[*] ayman.hoblos@femto-st.fr

**Abstract:** A simple configuration of only $\lambda/9$ thick 2D metallic grating embedded within an electro-optic (EO) material (lithium niobate for instance) is proposed and theoretically studied to act as an EO modulator. On the first hand, this grating is used as an interdigitated comb to apply a very high and spatially periodic modification of the electrostatic field. On the other hand, the grating is designed to exhibit a Fano-like resonance in the NIR spectral range. This resonance is used to confine the electromagnetic field inside the EO material leading to an intrinsic enhancement of the EO effect. Extensive numerical simulations are performed to optimize the geometry in agreement with technological fabrication constraints. We achieved a local field factor of 24.5 leading to a local index modification $\Delta n$ as large as 1 for 1 V applied voltage. This allows a modulation sensitivity of 14.35 nm/V (2000 times larger than the state of the art) together with a resonance depth= of 60% and a driving voltage of only 75 mV opening the way to the fabrication of ultra-thin low driving voltage EO devices.



## 1. Introduction

Electro-optical (EO) modulators required to convert electrical signals into optical informations are crucial and in very high demand for most optical-based devices and telecommunication systems [1, 2]. In this context, lithium niobate ($LiNbO_3$) is known as one of the best candidate for EO devices due to its important physical properties, notably its high EO coefficients [3–5]. It offers a wide transparency band, which opens the range to applications from visible to mid-infrared. The dominance of $LiNbO_3$ in EO technologies is related to its higher Curie temperature compared to other EO materials, which makes it robust to temperature variation and harsh environments.

The efficiency of an EO modulator is linked to the electric voltage needed to drive the modulator and to the footprint of the device that can be assessed with the $V_d \cdot L$ figure of merit, where $V_d$ is the driving voltage and $L$ the active length. In general, commercial EO modulators made of $LiNbO_3$ and based on a Mach-Zehnder interferometer (MZI) present a half wave voltage between 3 V [6] and 1 V [7] with an active length larger than one centimeter.

After the emergence of thin-film lithium niobate (TFLN) [8, 9], a new era in photonics technology has begun, leading to EO devices with reduced footprint and driving voltage. In the last couple of years, the progress remains improving in order to conceive EO modulators with lower half wave voltage ($V_\pi$) and larger bandwidth taking advantage of TFLN [10–12]. In [10], they achieved a 1 V driving voltage and 110 GHz bandwidth in a TFLN-modulator that works in dual-polarization, enabling a record single-wavelength 1.96 Tb/s net data rate. However, Weiss *et al.* [12] proposed a plasmonic nanoscale metasurface array coupled with a TFLN and reach a wavelength tunablity of 3 nm for a 50 V peak-to-peak voltage difference. Generally, the voltage-length product ($V_\pi \cdot L$) of the TFLN modulator is 1.5 to 3 V·cm [13, 14], which is considerably lower than that of commercial LN modulators (15 V·cm) [1] at telecom wavelengths.

Photonic Crystals (PhC) can exalt EO interactions and gain even more than an order of magnitude on the figure of merit compared to MZ-based architectures [15]. Moreover, PhC architecture can thereby shrink down the device footprint which reduces its capacitance and the required switching voltage. The emergence of PhC-based devices has increased the integration of photonic devices to meet the requirements of embedded technologies and become competitive with electronic devices.

A $LiNbO_3$ PhC modulator was proposed since 2007 to enhance the EO effect by locally confining the electromagnetic field when a Bloch mode is excited within the PhC [16]. This becomes relevant when the group velocity of this Bloch mode is very small. In this case, the time interaction between light and matter grows significantly leading to exacerbate all the intrinsic non-linear coefficients of the considered material, among others, the second order susceptibility term $\chi^{(2)}$ involved in the EO effect. Such enhancement was experimentally [17] verified and theoretically explained. Thereby, a new generation of EO modulators [18], pyroelectric detectors [19] or Second Harmonic Generation (SHG) devices [20] were proposed, fabricated and characterized validating the principle of this enhancement. Meanwhile, dark Fano resonances, also know by optical bound state in the continuum (BIC), were also explored in order to exacerbate the EO effect [21]. It provides an excellent electromagnetic field confinement essential to enhance the EO effect surpassing a conventional guided resonance [22].

Here, we proposed a simple Ag-$LiNbO_3$ configuration based on the excitation of a Fano-like resonance at $\lambda_{res} = 1530$ nm insuring the electromagnetic field confinement required to enhance the host medium EO coefficient. The geometry of the structure is inspired by the one studied in [23] where a miniaturized acousto-optic modulator based on sub-wavelength structures presenting simultaneously a photonic and phononic resonance has been proposed and studied demonstrating a strong optical modulation at near infrared wavelengths.

## 2. Proposed Structure

Unlike most common modulators, we propose a configuration operating in the $\Gamma$ direction (out-of-plane illumination at normal incidence), which allows us to illuminate the structure in free space and overcome the optical losses that occur by an in-plane illumination such as the injection losses and the propagation losses, as it is the case for MZI-based modulators. Our EO modulator, as shown in Fig.1(a), is based on a simple configuration of a 2D metallic grating of thickness $h = \lambda/9$, embedded in the $LiNbO_3$ in order to take advantage of the confinement of the electromagnetic field induced by our Fano resonance. On one hand, this grating is used as an interdigital comb to apply a very high and spatially periodic variation of the electrostatic field leading to an enhancement of the EO effect and improvement of the EO sensitivity. On the other hand, the grating is designed to optically exhibit a Fano type resonance in the NIR spectral range. Our proposed structure relies on a 1D PhC structure with a grating lattice $p$. The unbalance between the two $LiNbO_3$ cavities with two different widths $W_1$ and $W_2$ creates a mismatch between the volume of the cavities and allow us to generate the well-known $\pi$-resonance also known as phase-resonance. The origin of the optical resonance appearing on the transmission spectrum through the structure has been discussed in [24]. In order to take advantage of the larger EO coefficient of the $LiNbO_3$, the applied voltage and electromagnetic field must be oriented parallel to the crystallographic $Z-$axis of the $LiNbO_3$, which requires an $X-$ or $Y-$cut $LiNbO_3$ slab. In the following, we will consider an $X-$cut $LiNbO_3$ structure and assume the $LiNbO_3$ extraordinary refractive index $n_e = 2.2472$ to be constant in the spectral range of interest.

In order to adapt the geometry, extensive FDTD (Finite Difference Time Domain) simulations with a custom code were performed to obtain resonance in the NIR spectral range with the highest Q-factor and the largest resonance depth (RD) corresponding to a maximum modulation amplitude. A uniform 2D mesh with a mesh size of $\Delta x = \Delta y = 2$ nm is applied to describe the structure. We consider an infinitely periodic structure in the $x$ direction by applying the

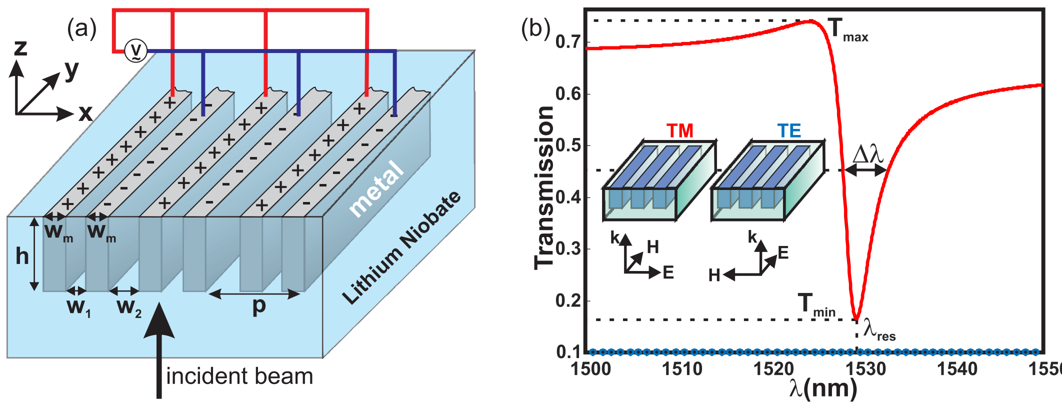


Fig. 1. (a)Schematic of the proposed structure showing its geometrical parameters and (b) transmission spectra for TE polarization presented by blue circles and by solid red line for the TM-polarized incident plane waves. The geometrical parameters are: $h$ = 170nm, $p$ = 650nm, $W_1$ = 150nm, $W_m$ = 120nm. The refractive index of $LiNbO_3$ is fixed to $n_e$ = 2.2472 and the metal is silver.

Bloch periodic boundary conditions, and perfectly matched layer (PML) conditions are used as absorbing boundary conditions to numerically truncate the substrate and superstrate media. Approximately 1 million iterations are considered for a single calculation to achieve the stopping criteria (steady states). All geometrical parameters were varied taking into account the fabrication constraints (aspect ratio $AR = h/min(W_m, W_1, W_2)$ smaller than 2 and slit width larger than 80$nm$). The geometrical parameters of the optimized structure are: $h$ = 170nm, $p$ = 650 $nm$, $W_1$ = 150nm, $W_m$ = 120nm. Different metals were also studied (Ag, Al, Pt, Au) for the electrodes, showing better results with silver. The latter presents the lowest optical absorption losses. Its dielectric properties are adapted to [25] through a Drude critical points model [26].

Fig.1(b) shows a typical transmission spectrum of light through the structure for the two linear polarization states (TE and TM). As expected, the slit structure behaves as a metallic grid polarizer with axis perpendicular to the slit direction. Consequently, only the $Ox$ incident polarization can be transmitted. The resonance depth (RD) and the quality factor (Q-factor) are defined from this spectrum by: $RD = \frac{T_{max} - T_{min}}{T_{max}}$ and $Q = \frac{\lambda_{res}}{\Delta\lambda}$. Their values, respectively 77% and 318 for the resonance at $\lambda_{res} = 1529.6$ $nm$, are above the experimentally required threshold values.

## 3. Results and Discussions

In order to enhance the EO effect in $LiNbO_3$, the electric field must overlap with the optical mode in the $LiNbO_3$, in other words, the electric field and the electromagnetic field has to be confined in the $LiNbO_3$ substrate leading to a dielectric mode and to the enhancement of the EO coefficient $r_{33}$ by a factor $F_{opt}$ as described in equation 1, the expression of the local EO effect [16]:

$$\Delta n_e(x, z) = -\frac{1}{2} n_e^3 r_{33} F_{opt}^2(x, z) E_{es}(x, z), \quad (1)$$

where $F_{opt}(x, z)$ is the local optical field factor defined by

$$F_{opt}(x, z) = \frac{|\vec{E}(x, z)|_{structure}}{|\vec{E}|_{bulk}}, \quad (2)$$

where $|\vec{E}|_{bulk}$ is the amplitude of the homogeneous E-field in the bulk $LiNbO_3$ substrate (without PhC) and $|\vec{E}(x,z)|_{structure}$ is the local amplitude of the E-field in the studied PhC structure. To confirm the existence of a dielectric mode and then derive the optical field factor $F_{opt}$, we calculate the electric field distribution at the resonance wavelength using a 2D-FDTD custom code. As shown in Fig.2(a), the normalized electric field intensity reaches its maximum at the corners of the electrodes and inside the $LiNbO_3$ between the two electrodes leading to a dielectric mode, which is consistent with the conditions required to enhance the EO effect. Based on the optical field factor definition given in Eq.2, we reach a maximum of $F^2_{opt}(x,z) = 1100$, which corresponds to a variation of the refractive index in the PhC structure up to 1100 times higher than that of the bulk structure. The normalization has been established with the same FDTD code and the same configuration of the calculation window without the nanostructure (periodic metallic grid). However, as described in Eq.1, the EO sensitivity depends on $F_{opt}(x,z)$ and electrostatic field distribution through $E_{es}(x,z)$.

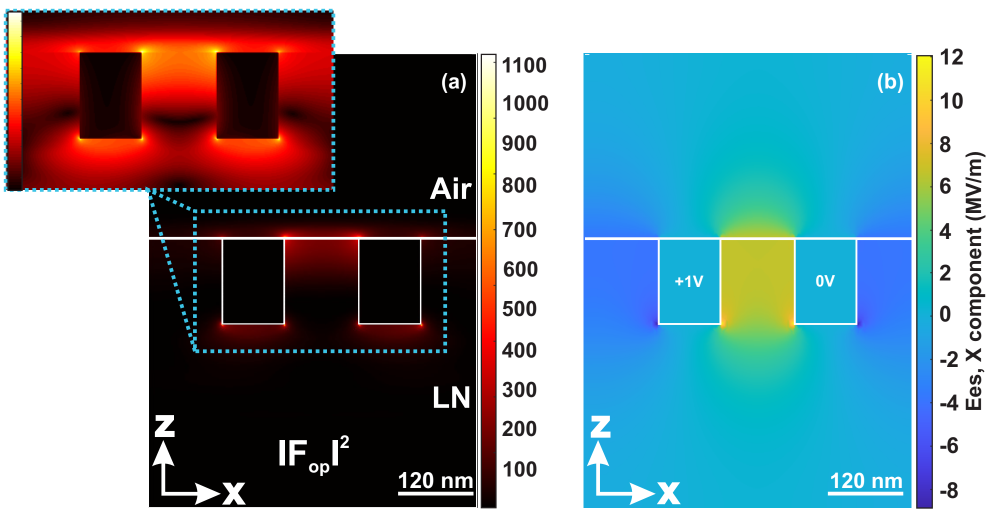


Fig. 2. (a) Spatial distribution of the normalized electric field intensity (or $F^2_{opt}(x,z)$) at $\lambda_{res}$ = 1529.6 nm. The white lines correspond to the structure edges. The zoom-in made over the highlighted rectangular zone on the left shows the electric field intensity to the power 0.4 to enhance the color contrast and presents clearly the electric field distribution in this zone. (b) Electrostatic field distribution (only the x-component) when a potential difference of 1V is applied between two consecutive electrodes.

After the estimation of $F_{opt}$ distribution, we moved to the calculation of the electrostatic field distribution $E_{es}$(x,z) in order to complete the missing values for the estimation of the EO effect of the proposed structure.

As previously explained, the applied electrostatic field $E_{es}$(x,z) is polarized along the x-directions which corresponds to the crystallographic Z-axis for a X-cut $LiNbO_3$ wafer in order to benefit from the highest EO coefficient of $LiNbO_3$ ($r_{33}$). For this reason, we will only consider in our calculations the X-components of $E_{es}$ since it will involve the highest EO coefficient of $LiNbO_3$ ($r_{33}$). Similarly, we will only focus on the electrostatic field confined inside the $LiNbO_3$ and not in the air, since the EO effect occurs only in the EO material ($LiNbO_3$ in our case). Indeed, no electrostatic field apart from the one in $LiNbO_3$ will contribute to the EO effect.

The same structure was modeled to solve the Poisson equation when a voltage of 1 V is applied between the two consecutive electrodes. Thus, COMSOL multiphysics software was used to this end by integrating periodic boundary conditions in the x-direction and Dirichlet boundary conditions for the up and down limits of the calculation window. In addition, a very fine mesh, based on Delaunay triangulation, was applied in order to minimize the numerical errors when interpolating the $E_{\text{es}}$(x,z) values over the regular square grid used in the FDTD simulations. The x-component of the electrostatic field presented in Fig.2(b) is showing a maximum value between the two electrodes and in the electrode corners immersed in $LiNbO_3$. It varies between $12 \times 10^6$ V/m and $-8.2 \times 10^6$ V/m, values that are slightly larger than

$$\frac{V}{W_1} = \frac{1}{150 \times 10^{-9}} = 6.67 \times 10^6\ V/m, \tag{3}$$

and

$$\frac{-V}{W_2} = \frac{-1}{260 \times 10^{-9}} = -3.85 \times 10^6\ V/m, \tag{4}$$

respectively. This difference comes from the presence of electrode corners (90°) that induces an enhancement of the electric field due to a well-known "antenna effect" that was widely studied both theoretically [27, 28] and experimentally [29, 30].

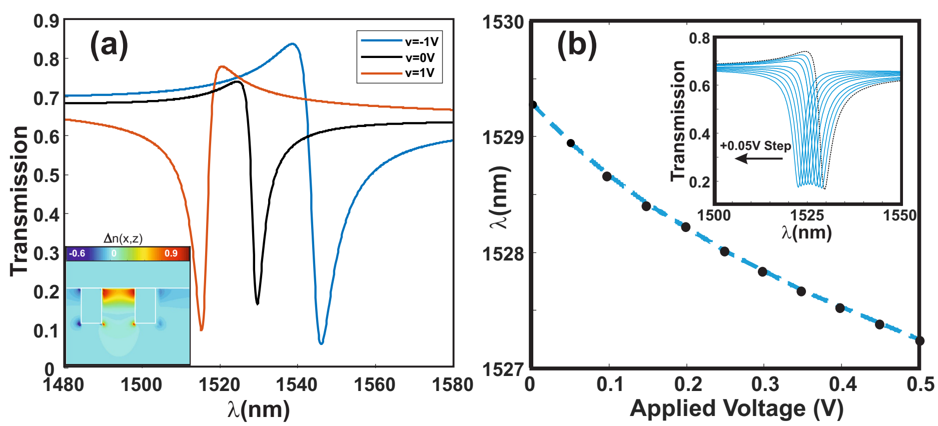


Fig. 3. (a) Shift of the resonance induced by an applied voltage of 1 V (in red) and −1 V (in blue). In black, the transmission spectrum of structure before applying an electric voltage. Inset: the local refractive index distribution for 1 V applied voltage. (b) The evolution of the resonance wavelength with respect to the applied voltage. Inset in blue the transmission spectra of the structure for different electric voltage going from 0 V to 0.5 V with a step of 0.05 V and in black the transmission spectrum of the structure for 0 V.

To highlight the mechanism of modulation, we started by estimating the sensitivity of the structure as response of an applied voltage. To do so, we compute the electrostatic field distribution for an applied voltage of 1 V and −1 V using COMSOL and inject these values with the optical field factor distribution into Eq.1 in order to calculate the resonance shift by FDTD. In Fig.3(a), we present the calculated three transmission spectra pointing out the resonance shift induced by 1 V (in red) and −1 V (in blue) applied voltage. More details about the resonances are summarized in Table 1.

For just 1 V applied voltage, the resonance (in red) shift to 1515.293 nm with a Q-factor of 252 and a RD of 87.3%. However, with a −1 V applied voltage, the resonance (in bleu) shift to 1546.02 nm with a Q-factor of 135 and a RD of 92.4%. Despite the larger shift with a −1 V applied voltage, the decrease in the Q-factor of the resonance is directly linked to a lower optical field factor compared to the other resonance (with an applied voltage of 1 V). In the following,

Table 1. Details about resonances in Fig.3(a).

| ΔV | $\lambda_{res}$ | Q-Factor | RD |
|---|---|---|---|
| 0 V | 1529.652 nm | 318 | 77.3% |
| 1 V | 1515.293 nm | 252 | 87.3% |
| −1 V | 1546.02 nm | 135 | 92.4% |

the modulation performance of the structure will be studied only with a positive applied voltage so we can benefit as much as possible from the EO enhancement of the proposed structure.

A sensitivity of 14.35 nm/V is estimated, which is 2000 times higher than the one recently achieved by Wang *et al.* [31]. The shift of the resonance wavelength with respect to the applied voltage is presented in Fig.3(b). Similarly, every point is computed by a couple of COMSOL-FDTD simulations. The trend of the curve with respect to the applied electric voltage is quasi-linear.

To end up with the modulation performance of the structure, we present in Fig.4 the optical response of the structure with respect to the applied voltage. We considered a light detector operating at the resonance wavelength, and we deduce the transmitted light for each applied voltage. We clearly see that we reach a permanent state for an applied voltage V=0.2 V. This means that our structure requires a driving voltage ($V_d$) as low as 0.2 V in order to go from the ON to the OFF states. In order to improve the modulation of the structure, one can consider the highlighted red zone where the transmission variation as function of the applied voltage is linear. We conclude with a minimized driving voltage $V_d$ = 0.075 V and an RD = 60% instead of $V_d$ = 0.2 V and an RD = 80% if we consider the complete modulation zone presented in Fig.4.

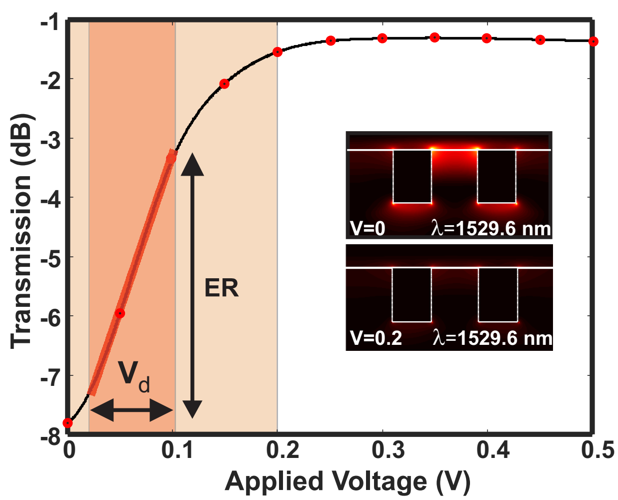


Fig. 4. The optical response of the structure with respect to the applied voltage. Inset: the electric field amplitude at the ON and OFF state for V= 0 V and 0.2 V, respectively.

In order to be more realistic, we study the effect of a finite structure with a finite number of period on its optical response. For this purpose, 2D-FDTD simulations are performed to evaluate the normalized zero-order transmission spectra of the structure with a finite number of periods and the previously determined parameters. The Bloch periodic boundary condition are replaced by perfectly matched layer boundary conditions in order to simulate the finite structure with a uniform mesh size of $\Delta_x = \Delta_z = 10$ nm in the $x$ and $z$ directions instead of 2 nm in order to speed up our simulations. The larger mesh size considered in our simulations will induce a shift of the resonance wavelength according to [32]. The structure is illuminated by a Gaussian beam whose size is fixed at 100 $\mu m$.

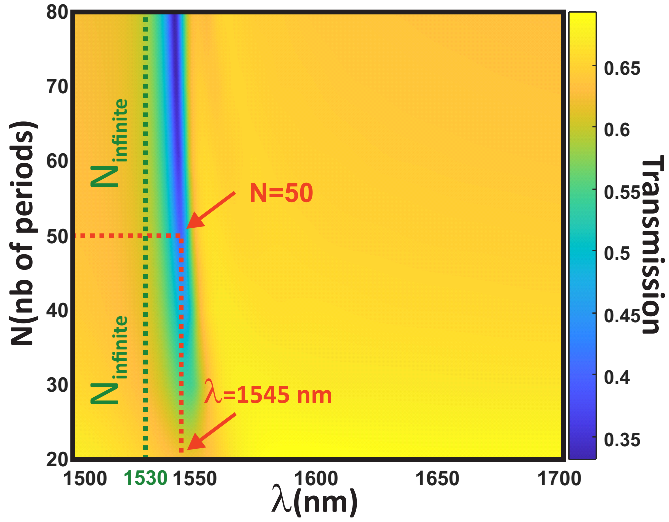


Fig. 5. Normalized transmission with respect to the number of periods. The dashed green line indicates the resonance position for an infinitely periodic structure, while the dashed red line refers to the resonance position, for 50 periods, where the RD and the Q factor of the resonance become sufficient for modulation.

The 2D-FDTD simulations are conducted by varying the number of periods, going from 20 periods to 80 periods. The result is presented in details in Fig.5 and table 2. On one hand, Fig.5 presents the evolution of the transmission with respect to the number of period. Going from 20 periods to 80 periods, the resonance wavelength shift from 1549 nm to 1543 nm. This is reasonable since it converges to the resonance position of the infinitely periodic structure denoted by the green dashed line. Admitting that a minimum RD of 40% is necessary to ensure a proper modulation, we note that starting from 50 periods, the resonance properties become sufficiently relevant to ensure the good modulation thanks to its significant RD and Q factor. This corresponds to a footprint of the structure as small as about $L$=32.5 µm. On the other hand, the table 2 shows the characteristics of the resonances for each number of periods. Similarly to what is presented in Fig.5, starting from 50 periods, the variation of the resonance properties becomes very small, revealing the convergence to almost stable values.

Table 2. Details of the resonance properties with respect to the number of periods N.

| N | $\lambda_{res}$ | Q-Factor | RD |
|---|---|---|---|
| 20 | 1548.80 nm | 56.6 | 10.26% |
| 30 | 1547.08 nm | 126.3 | 19.6% |
| 40 | 1546.04 nm | 164.2 | 30.1% |
| 50 | 1545 nm | 217.47 | 39.28% |
| 60 | 1544.76 nm | 268.84 | 44.98% |
| 70 | 1544.16 nm | 273.73 | 47.59% |
| 80 | 1543.65 nm | 273.97 | 49.73% |

In order to compare the performance of our modulator with other modulators available in the literature, we rely on the voltage-length product of the modulator expressed by the product $V_d$·L, where $V_d$ is the driving voltage of our structure and $L$ the active length of the structure. If we consider a finite structure with 60 periods ($L$ = 39 µm) and $V_d$ 0.075 V or 0.2 V, we reach a voltage-length product of about $2.925 \times 10^{-4}$ V·cm or $7.8 \times 10^{-3}$ V·cm, respectively. In both cases, our voltage-length product is more than two order of magnitude smaller than other LN EO modulators [13, 15, 33]. In addition, a comparison table was provided in table 3 to benchmark all

Table 3. Comparison of modulator metrics: switching voltage, voltage-length product (V-L), ER and modulation tuning.

| Type | Switching Voltage (V) | V-L (V·cm) | ER (dB) | Modulation Tuning | Reference |
|---|---|---|---|---|---|
| MZI | 1.4 | 2.8 | 30 | N/A | [13] |
| MZI | 2.3 | 2.3 | 30 | N/A | [13] |
| MZI | 4.4 | 2.2 | 30 | N/A | [13] |
| Micro-Ring | 9 | 1.8 | 10 | 7 pm/V | [31] |
| Metasurface | 100 | N/A | 4.7 | 20 nm/V (GMR) | [34] |
| Our structure | 0.075/ 0.2 | $2.925 \times 10^{-4}$ / $7.8 \times 10^{-3}$ | 4.7/ 6.7 | 14.35 nm/V | This work |

relevant metrics.

## 4. Conclusion

Our theoretical studies reveal the opportunity to develop an EO modulator with a minimized driving voltage $V_d$ = 75 mV and a reduced footprint of $L$ = 39 µm based on the well-known EO effect in $LiNbO_3$, Pockels effect. We achieved a high sensitivity up to 14.35 nm/V and a minimized voltage-length product of about $2.925 \times 10^{-4}$ V·cm with our 2D metasurface-based proposed structure. We reach a new horizon since, for the best of our knowledge, the deduced $V_d.L$ is the lowest in the literature and in the market.

## 5. Acknowledgements

Several computations have been performed on the supercomputer facilities of the "Mésocentre de calcul de Franche-Comté". This work has been partially supported by the EIPHI Graduate School (contract ANR-17-EURE-0002) and by the ANR-CNRS Astrid Maturation EsencyaIMAT under the number ANR-19-ASMA-0003-01.

## Disclosures

The authors declare no conflicts of interest.

## Data availability

Data underlying the results presented in this paper are not publicly available at this time but may be obtained from the authors upon reasonable request.

## References

1. E. L. Wooten, K. M. Kissa, A. Yi-Yan, E. J. Murphy, D. A. Lafaw, P. F. Hallemeier, D. Maack, D. V. Attanasio, D. J. Fritz, G. J. McBrien, and D. E. Bossi, “A review of lithium niobate modulators for fiber-optic communications systems,” IEEE J. selected topics Quantum Electron. **6**, 69–82 (2000).
2. D. A. Miller, “Attojoule optoelectronics for low-energy information processing and communications,” J. Light. Technol. **35**, 346–396 (2017).

3. M. Jacques, A. Samani, D. Patel, E. El-Fiky, M. Morsy-Osman, T. Hoang, M. G. Saber, L. Xu, J. Sonkoly, M. Ayliffe, and D. V. PLANT, “Modulator material impact on chirp, dsp, and performance in coherent digital links: comparison of the lithium niobate, indium phosphide, and silicon platforms,” Opt. Express **26**, 22471–22490 (2018).
4. T. Ren, M. Zhang, C. Wang, L. Shao, C. Reimer, Y. Zhang, O. King, R. Esman, T. Cullen, and M. Lončar, “An integrated low-voltage broadband lithium niobate phase modulator,” IEEE Photonics Technol. Lett. **31**, 889–892 (2019).
5. M. Wang, J. Li, K. Chen, and Z. Hu, “Thin-film lithium niobate electro-optic modulator on a d-shaped fiber,” Opt. Express **28**, 21464–21473 (2020).
6. “ixblue company,” https://photonics.ixblue.com/products-list/intensity-modulators.
7. “Hyperlight company,” https://hyperlightcorp.com/.
8. G. Poberaj, M. Koechlin, F. Sulser, A. Guarino, J. Hajfler, and P. Günter, “Ion-sliced lithium niobate thin films for active photonic devices,” Opt. Mater. **31**, 1054–1058 (2009).
9. G. Poberaj, H. Hu, W. Sohler, and P. Guenter, “Lithium niobate on insulator (lnoi) for micro-photonic devices,” Laser & Photonics Rev. **6**, 488–503 (2012).
10. M. Xu, Y. Zhu, F. Pittalà, J. Tang, M. He, W. C. Ng, J. Wang, Z. Ruan, X. Tang, M. Kuschnerov, L. Liu, S. Yu, B. Zheng, and X. Cai, “Dual-polarization thin-film lithium niobate in-phase quadrature modulators for terabit-per-second transmission,” Optica **9**, 61–62 (2022).
11. G. Chen, K. Chen, R. Gan, Z. Ruan, Z. Wang, P. Huang, C. Lu, A. P. T. Lau, D. Dai, C. Guo, and L. Liu, “High performance thin-film lithium niobate modulator on a silicon substrate using periodic capacitively loaded traveling-wave electrode,” APL Photonics **7**, 026103 (2022).
12. A. Weiss, C. Frydendahl, J. Bar-David, R. Zektzer, E. Edrei, J. Engelberg, N. Mazurski, B. Desiatov, and U. Levy, “Tunable metasurface using thin-film lithium niobate in the telecom regime,” ACS Photonics **9**, 605–612 (2022).
13. C. Wang, M. Zhang, X. Chen, M. Bertrand, A. Shams-Ansari, S. Chandrasekhar, P. Winzer, and M. Lončar, “Integrated lithium niobate electro-optic modulators operating at cmos-compatible voltages,” Nature **562**, 101–104 (2018).
14. A. N. R. Ahmed, S. Nelan, S. Shi, P. Yao, A. Mercante, and D. W. Prather, “Subvolt electro-optical modulator on thin-film lithium niobate and silicon nitride hybrid platform,” Opt. letters **45**, 1112–1115 (2020).
15. M. Li, J. Ling, Y. He, U. A. Javid, S. Xue, and Q. Lin, “Lithium niobate photonic-crystal electro-optic modulator,” Nat. Commun. **11**, 1–8 (2020).
16. M. Roussey, F. I. Baida, and M.-P. Bernal, “Experimental and theoretical observations of the slow-light effect on a tunable photonic crystal,” JOSA B **24**, 1416–1422 (2007).
17. S. Diziain, J. Amet, F. I. Baida, and M.-P. Bernal, “Optical far-field and near-field observations of the strong angular dispersion in a lithium niobate photonic crystal superprism designed for double (passive and active) demultiplexer applications,” Appl. Phys. Lett. **93**, 261103 (2008).
18. M. Roussey, M.-P. Bernal, N. Courjal, D. Van Labeke, F. Baida, and R. Salut, “Electro-optic effect exaltation on lithium niobate photonic crystals due to slow photons,” Appl. physics letters **89**, 241110 (2006).
19. M.-P. Bernal, J. Amet, J. Safioui, F. Devaux, M. Chauvet, J. Salvi, and F. Baida, “Pyroelectric control of the superprism effect in a lithium niobate photonic crystal in slow light configuration,” Appl. Phys. Lett. **98** (2011).
20. R. M. Roth, N. C. Panoiu, M. M. Adams, R. M. Osgood, C. C. Neacsu, and M. B. Raschke, “Resonant-plasmon field enhancement from asymmetrically illuminated conical metallic-probe tips,” Opt. express **14**, 2921–2931 (2006).
21. A. Hoblos, M. Suarez, N. Courjal, M.-P. Bernal, and F. I. Baida, “Excitation of symmetry protected modes in a lithium niobate membrane photonic crystal for sensing applications,” OSA Continuum **3**, 3008–3018 (2020).
22. S. Fan and J. D. Joannopoulos, “Analysis of guided resonances in photonic crystal slabs,” Phys. Rev. B **65**, 235112 (2002).
23. V. Laude, A. Belkhir, A. F. Alabiad, M. Addouche, S. Benchabane, A. Khelif, and F. I. Baida, “Extraordinary nonlinear transmission modulation in a doubly resonant acousto-optical structure,” Optica **4**, 1245–1250 (2017).
24. D. C. Skigin and R. A. Depine, “Transmission resonances of metallic compound gratings with subwavelength slits,” Phys. review letters **95**, 217402 (2005).
25. E. D. Palik, *Handbook of Optical Constants of Solids. Acad. Press.,* (Academic, 1985).
26. A. Vial, “Implementation of the critical points model in the recursive convolution method for modelling dispersive media with the finite-difference time domain method,” J. Opt. A: Pure Appl. Opt. **9**, 745 (2007).
27. F. Demming, J. Jersch, K. Dickmann, and P. Geshev, “Calculation of the field enhancement on laser-illuminated scanning probe tips by the boundary element method.” Appl. Phys. B: Lasers & Opt. **66** (1998).
28. S. Kawata and V. Shalaev, “Advances in nano-optics and nano-photonics,” (2006).
29. F. H‘Dhili, R. Bachelot, G. Lerondel, D. Barchiesi, and P. Royer, “Near-field optics: Direct observation of the field enhancement below an apertureless probe using a photosensitive polymer,” Appl. Phys. Lett. **79**, 4019–4021 (2001).
30. R. Bachelot, F. H‘Dhili, D. Barchiesi, G. Lerondel, R. Fikri, P. Royer, N. Landraud, J. Peretti, F. Chaput, G. Larnpel, J. Boilot, and K. Lahlil, “Apertureless near-field optical microscopy: A study of the local tip field enhancement using photosensitive azobenzene-containing films,” J. Appl. Phys. **94**, 2060–2072 (2003).
31. C. Wang, M. Zhang, B. Stern, M. Lipson, and M. Lončar, “Nanophotonic lithium niobate electro-optic modulators,” Opt. express **26**, 1547–1555 (2018).
32. A. Hoblos, M. Suarez, B. Guichardaz, N. Courjal, M.-P. Bernal, and F. I. Baida, “Revealing photonic symmetry-protected modes by the finite-difference-time-domain method,” Opt. Lett. **45**, 2103–2106 (2020).

33. M. He, M. Xu, Y. Ren, J. Jian, Z. Ruan, Y. Xu, S. Gao, S. Sun, X. Wen, L. Zhou, L. Liu, C. Guo, H. Chen, S. Yu, L. Liu, and X. Cai, "High-performance hybrid silicon and lithium niobate mach–zehnder modulators for 100 gbit s- 1 and beyond," Nat. Photonics **13**, 359–364 (2019).
34. I.-C. Benea-Chelmus, S. Mason, M. L. Meretska, D. L. Elder, D. Kazakov, A. Shams-Ansari, L. R. Dalton, and F. Capasso, "Gigahertz free-space electro-optic modulators based on mie resonances," Nat. Commun. **13**, 1–9 (2022).